Atmospheric Rivers over the Northwestern Pacific: Climatology and Interannual Variability

YOUICHI KAMAE

Faculty of Life and Environmental Sciences, University of Tsukuba, Tsukuba, Ibaraki, Japan, and Scripps Institution of Oceanography, University of California San Diego, La Jolla, California

WEI MEI

Department of Marine Sciences, University of North Carolina at Chapel Hill, Chapel Hill, North Carolina

SHANG-PING XIE

Scripps Institution of Oceanography, University of California San Diego, La Jolla, California

MOEKA NAOI

College of Geoscience, School of Life and Environmental Sciences, University of Tsukuba, Tsukuba, Ibaraki, Japan

HIROAKI UEDA

Faculty of Life and Environmental Sciences, University of Tsukuba, Tsukuba, Ibaraki, Japan

ABSTRACT

Atmospheric rivers (ARs), conduits of intense water vapor transport in the midlatitudes, are critically important for water resources and heavy rainfall events over the west coast of North America, Europe, and Africa. ARs are also frequently observed over the northwestern Pacific (NWP) during boreal summer but have not been studied comprehensively. Here the climatology, seasonal variation, interannual variability, and predictability of NWP ARs (NWPARs) are examined by using a large ensemble, high-resolution atmospheric general circulation model (AGCM) simulation and a global atmospheric reanalysis. The AGCM captures general characteristics of climatology and variability compared to the reanalysis, suggesting a strong sea surface temperature (SST) effect on NWPARs. The summertime NWPAR occurrences are tightly related to El Niño–Southern Oscillation (ENSO) in the preceding winter through Indo–western Pacific Ocean capacitor (IPOC) effects. An enhanced East Asian summer monsoon and a low-level anticyclonic anomaly over the tropical western North Pacific in the post–El Niño summer reinforce low-level water vapor transport from the tropics with increased occurrence of NWPARs. The strong coupling with ENSO and IPOC indicates a high predictability of anomalous summertime NWPAR activity.

1. Introduction

Atmospheric rivers (ARs), filament-shaped conduits of water vapor transport from the tropics to the middle and high latitudes, are major transient features of the global hydrological cycle (Zhu and Newell 1998; Ralph et al. 2004; Gimeno et al. 2014). They occur within warm conveyor belts of extratropical cyclones and are frequently observed over midlatitude oceans (4–5 ARs are usually present at any time; Zhu and Newell 1998). ARs are of great importance in meridional water vapor transport (>90% of climatological water vapor transport at the midlatitudes is ascribed to ARs; Zhu and Newell 1998) despite their limited widths (typically 300–500 km). They have substantial impacts on human society in coastal regions and can cause floods and landslides when they make landfall.

Corresponding author: Youichi Kamae, kamae.yoichi.fw@u.tsukuba.ac.jp

Previous studies have examined the role of ARs in land hydrology (rainfall, snow accumulation, and ending droughts) over the west coast of North America (e.g., Bao et al. 2006; Neiman et al. 2008; Dettinger et al. 2011; Dettinger 2013; Payne and Magnusdottir 2014; Jackson et al. 2016), South America (Viale and Nuñez 2011), Europe (e.g., Lavers et al. 2012; Brands et al. 2017; Ramos et al. 2016), and Africa (Brands et al. 2017; Gimeno et al. 2016). Recent studies pointed out that near-surface strong winds associated with ARs also have important socioeconomic impacts (Khouakhi and Villarini 2016; Waliser and Guan 2017). Representation of ARs in weather forecast models is greatly important for prediction of AR-related extreme events (e.g., Wick et al. 2013; Lavers et al. 2014; Nayak et al. 2014). Gimeno et al. (2016) provided a comprehensive review on the mechanisms of atmospheric moisture transport including ARs. Guan and Waliser (2015) and Mundhenk et al. (2016, hereafter M16) examined climatology of AR frequency in global atmospheric reanalyses and revealed that ARs are not only concentrated in the central–eastern parts of the oceans but are also found over the northwestern Pacific (NWP).

Over East Asia, meridional water vapor transport from the tropics peaks in boreal summer (Knippertz and Wernli 2010) associated with the East Asian summer monsoon (EASM). The mei-yu–baiu (MB) rainband over China, the Korea Peninsula, and Japan during the summer monsoon season brings a large amount of rainfall (e.g., Ninomiya and Murakami 1987; Tao and Chen 1987; Ninomiya and Akiyama 1992; Sampe and Xie 2010). Seasonal variations of tropical forcing, the jet stream, and land–sea thermal contrast (Nitta 1987; Wang 1992; Kodama 1993; Ueda et al. 1995; Xie and Saiki 1999; Ueda 2005; Ding and Chan 2005; Sampe and Xie 2010) influence northward migration of the MB rainband, determining the timing of rainy season onset among southern to northern regions of the EASM (onset over southern China in early June and over the Korea Peninsula and Japan in July, and withdrawal in 1–2 months; e.g., Tao and Chen 1987; Lau and Yang 1997; Wang and LinHo 2002). During the MB rainy season, heavy rainfall events associated with anomalous low-level water vapor transport from the tropics have enormous socioeconomic impacts over East Asia (e.g., Matsumoto et al. 1971; Ninomiya 1980; Huang et al. 2007; Ninomiya and Shibagaki 2007; Manda et al. 2014). Figure 1 shows, as an example, a strong MB front accompanied with an AR-like enhanced southwesterly moisture transport (see section 2c) from the East China Sea and western North Pacific that caused heavy rainfall over western and central Japan. Miyatakogen (a station on the mountains between the Pacific and Japan Sea

coasts in Nagano Prefecture of central Japan) received a record-breaking daily rainfall of 267 mm on 19 July 2006 (Fig. 1c). Heavy rainfall events associated with AR-like moisture transport are not limited to the MB rainy season. Hirota et al. (2016) examined a heavy rainfall event of the autumn 2014 (after MB withdrawal) in Hiroshima that killed 75 people in widespread landslides and pointed out an importance of a filamentary transport of water vapor from Indochina as a background condition for the heavy rainfall. Over the NWP, detailed behavior of summertime ARs has not been examined, perhaps because the background water vapor is high, unlike the wintertime eastern North Pacific (see section 5). However, fluctuations of summertime AR activity over the NWP may affect the probability of East Asian extreme rainfall events.

El Niño–Southern Oscillation (ENSO) affects the interannual variability of wintertime AR landfalls over the west coast of North America via a meridional atmospheric teleconnection called the Pacific–North American pattern (e.g., Bao et al. 2006; Payne and Magnusdottir 2014). During El Niño winters, landfalling ARs increase over California and Central America as a result of equatorward shifts of the subtropical jet and storm track over the North Pacific. ENSO also affects the wintertime AR frequency over the NWP (more ARs over the subtropical western North Pacific during El Niño winters, and vice versa; Guan and Waliser 2015; M16). Over Europe, Lavers et al. (2012) showed that the wintertime landfalling ARs are closely related to the Scandinavian pattern (Mailier et al. 2006; Bueh and Nakamura 2007), which influences positions of the jet stream and storm track.

In contrast to winter, it is still unclear whether and how summertime AR variability is controlled by climate modes. The statistical relationship between ARs and climate modes is difficult to evaluate only from observations because of small sample sizes (i.e., global atmospheric reanalyses are typically only available since 1979) and dominant midlatitude atmospheric internal variability, limiting our ability to study the mechanisms. This study examines seasonal AR variation and interannual variability of summertime ARs over the NWP by using both long-term (since 1958) global reanalysis and high-resolution historical (since 1951) atmospheric general circulation model (AGCM) simulations. The large ensemble size of the latter contributes to increased signal-to-noise ratio in relationship between climate modes and midlatitude AR variability. Our results suggest a strong coupling of summertime AR activity with a major tropical mode, indicating high predictability. Section 2 describes data and methods including observations, large ensemble simulation, and AR detection
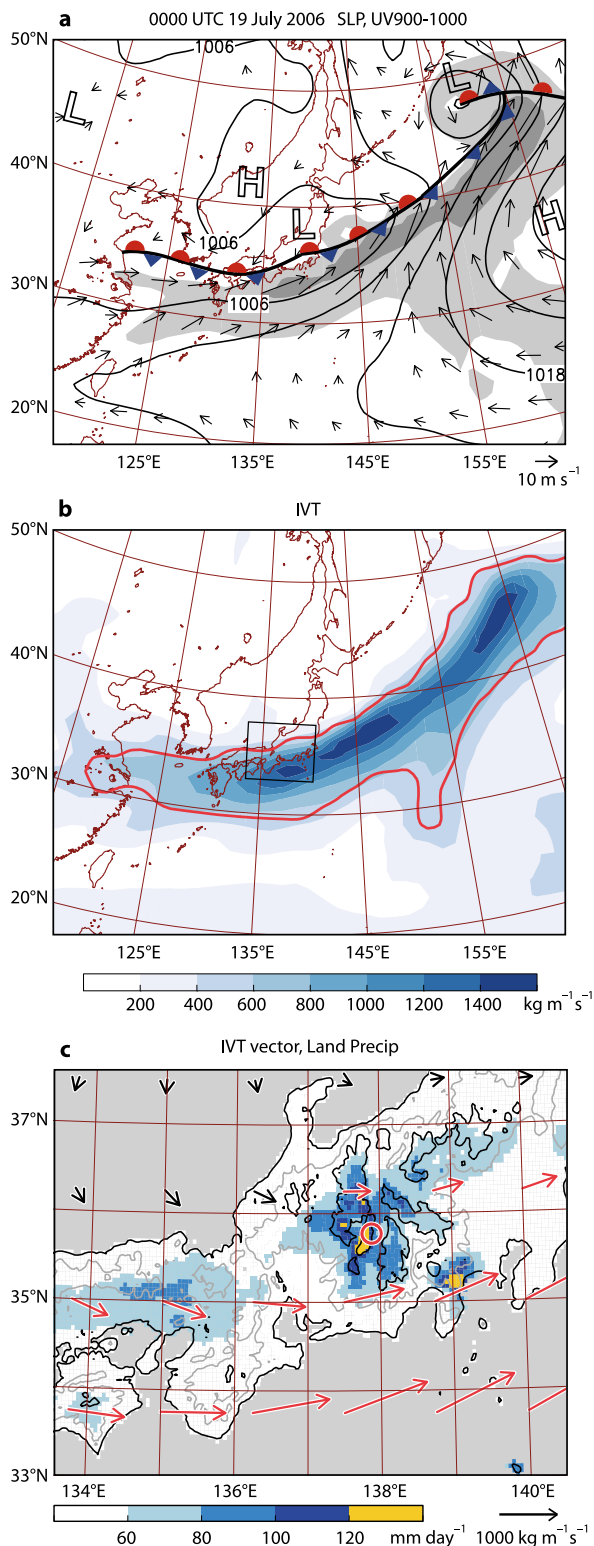
FIG. 1. An example of an AR in the western North Pacific detected by IVT in JRA-55. (a) Surface weather chart at 0000 UTC 19 Jul 2006. Contours represent sea level pressure (hPa). Vectors indicate horizontal wind ($m\,s^{-1}$) averaged between 900- and 1000-hPa levels. Light and dark shading indicate regions where absolute wind speeds exceed 10 and $20\,m\,s^{-1}$, respectively. (b) IVT ($kg\,m^{-1}\,s^{-1}$) and outline of a detected AR (red line; see section 2c for detail). Black rectangle represents the central Japan region shown in (c). (c) Land rainfall ($mm\,day^{-1}$) over central Japan on 19 Jul 2006 derived from a gridded ($0.05° \times 0.05°$ resolution) APHRODITE surface meteorological dataset (APHRO_JP V1207; Kamiguchi et al. 2010). Gray (400 m) and black (1200 m) contours indicate topography (ETOPO2v2; National Geophysical Data Center 2006). Arrows indicate IVT vector ($kg\,m^{-1}\,s^{-1}$). Red arrows indicate the regions where the AR exists. Red circle represents Miyatakogen station.

algorithm used in this study. Section 3 presents the climatology and seasonal variation of ARs based on global reanalysis and the ensemble simulation. Section 4 examines the relationships among the interannual variability of ARs over the NWP, sea surface temperature (SST), and atmospheric circulation patterns. In section 5, we present a summary and discussion.

2. Data and methods

a. Observations and reanalysis

We use the Japanese 55-year Reanalysis (JRA-55; Kobayashi et al. 2015) at $1.25° \times 1.25°$ spatial resolution to examine historical variation (for 1958–2010) in AR occurrence (see section 2c). Seasonal and interannual variations of ARs are compared with SST from HadISST (Rayner et al. 2003) at $1.0° \times 1.0°$ spatial resolution (for 1951–2010), precipitation from the Global Precipitation Climatology Project, version 2.2, at $2.5° \times 2.5°$ spatial resolution (for 1979–2010; Huffman et al. 2009), and surface and three-dimensional variables (sea level pressure, horizontal wind, and thickness) from JRA-55. The spatial resolution of ARs and atmospheric variables from JRA-55 is identical to those in large ensemble simulation (see sections 2b and 2c).

b. Large-ensemble simulation

In the midlatitudes, atmospheric internal variability greatly affects positions and behaviors of individual ARs (e.g., Hagos et al. 2016). The great importance of atmospheric internal variability results in a low signal-to-noise ratio in forced components of AR variability induced by historical radiative forcing, sea ice, and modes of SST variability including ENSO (see section 4a). In this study, we use an ensemble (10 member) historical simulation (for 1951–2010) with a high-resolution AGCM (Mizuta et al. 2017) to increase

the signal-to-noise ratio and capture the relationship between variability in AR occurrence and climate modes. The ensemble simulations were performed with the Meteorological Research Institute AGCM (MRI-AGCM), version 3.2 (Mizuta et al. 2012), at a horizontal spectral resolution with triangular truncation at wavenumber 319 and linear Gaussian grid (TL319; equivalent to 60-km mesh), with 64 vertical layers (Murakami et al. 2012). The AGCM was driven by observation-based SST and sea ice (Hirahara et al. 2014) and historical radiative forcing (greenhouse gases, aerosols, and ozone) for 1951–2010. For each member run, SST perturbations were added to the best estimate of SST to account for uncertainties in analysis (Hirahara et al. 2014). The perturbations are based on empirical orthogonal functions of the interannual variations of the SST analysis [see the appendix of Mizuta et al. (2017)]. Sea ice concentration was derived from a quadratic equation on the sea ice–SST relationship (Hirahara et al. 2014). The ensemble mean of the simulations can be regarded as approximations of forced atmospheric response to the radiative forcing, SST, and sea ice (Kamae et al. 2017). This dataset, called the Database for Probabilistic Description of Future Climate Change (d4PDF), is used to evaluate historical variations of atmospheric responses to global SST variability (Kamae et al. 2017). More details of the experimental setup and simulated climate variations can be found in Mizuta et al. (2017) and Kamae et al. (2017).

c. Detection of ARs

We use an AR detection algorithm developed by M16. The original source code was provided by B. D. Mundhenk (see the appendix of M16). We use 6-hourly atmospheric variables (specific humidity and horizontal wind) at $1.25° \times 1.25°$ spatial resolution from JRA-55 and d4PDF ensemble simulation. Previous studies used two different atmospheric variables, integrated water vapor (e.g., Ralph et al. 2004) and vertically integrated water vapor transport (IVT) between 1000 and 300 hPa (e.g., Lavers et al. 2012), to detect ARs from three-dimensional atmospheric fields (Gimeno et al. 2014; Guan and Waliser 2015; and references therein). IVT is determined as

$$\text{IVT} = \sqrt{\left(\frac{1}{g}\int_{1000}^{300} qu\,dp\right)^2 + \left(\frac{1}{g}\int_{1000}^{300} qv\,dp\right)^2},$$

where q is specific humidity, g is the acceleration due to gravity, and u and v are zonal and meridional wind, respectively. We refer anomalous IVT fields from its daily climatology (determined by long-term mean for 1958–2010 in JRA-55 and 1951–2010 in d4PDF, respectively) to exclude effects of background seasonal cycle of

tropospheric water vapor content. An anomalous IVT threshold of $140\,\text{kg}\,\text{m}^{-1}\,\text{s}^{-1}$ is used to detect AR-like water vapor transport. In previous studies, another IVT threshold (the 85th percentile in each grid) was employed for AR detection (e.g., Lavers et al. 2012; Nayak et al. 2014; Guan and Waliser 2015). The derived climatology and variability of North Pacific AR activity (Guan and Waliser 2015) were generally similar to those derived from the current method (see section 4 in M16). Next the identified water vapor transports with small area ($<7.8 \times 10^5\,\text{km}^2$) or short length ($<1500\,\text{km}$) or small length–width ratio (<1.325) are removed. In addition, east–west-oriented bands of IVT with a center of mass equatorward of 20°N are also removed because they are commonly found tropical moisture swells. More details of the detection algorithm are found in an appendix of M16. We adjust several parameters from the original code because the horizontal resolution of atmospheric variables from JRA-55 and d4PDF ($1.25° \times 1.25°$) is different from that used in M16 ($0.50° \times 0.67°$). The adjustments in the parameters affect resultant climatology of AR frequency (e.g., Guan and Waliser 2015), but its spatial pattern and interannual variability are qualitatively consistent among results from different parameter choices (see section 5).

Figure 1 shows an example of detected feature causing extreme heavy rainfall over Japan in July 2006 (see section 1). A meridionally elongated narrow moisture plume in the midlatitude western North Pacific is associated with 1) an extratropical cyclone (near Kamchatka) and associated cold front, similar to ARs in other parts of the North Pacific domain (e.g., Ralph et al. 2004; M16), and 2) an enhanced MB front over the Yellow Sea, the Korea Peninsula, and Japan. The latter is a unique feature compared to the wintertime North Pacific ARs. In the western North Pacific, individual detected features reveal complexity of shapes and associated synoptic weather patterns (Knippertz and Wernli 2010; M16; see the discussion in section 5 herein). This study mainly examines monthly and seasonal-mean statistics of AR frequency and associated large-scale climate variability modes. AR frequencies are calculated based on the number of 6-hourly periods during which an AR exists over a given grid point divided by the total number of periods.

3. Climatology and seasonal variation of AR occurrence

This section examines seasonal AR climatology in d4PDF and compares them with the global reanalysis to validate the AGCM simulation. Figure 2 compares AR climatology in the Northern Hemisphere in JRA-55 and
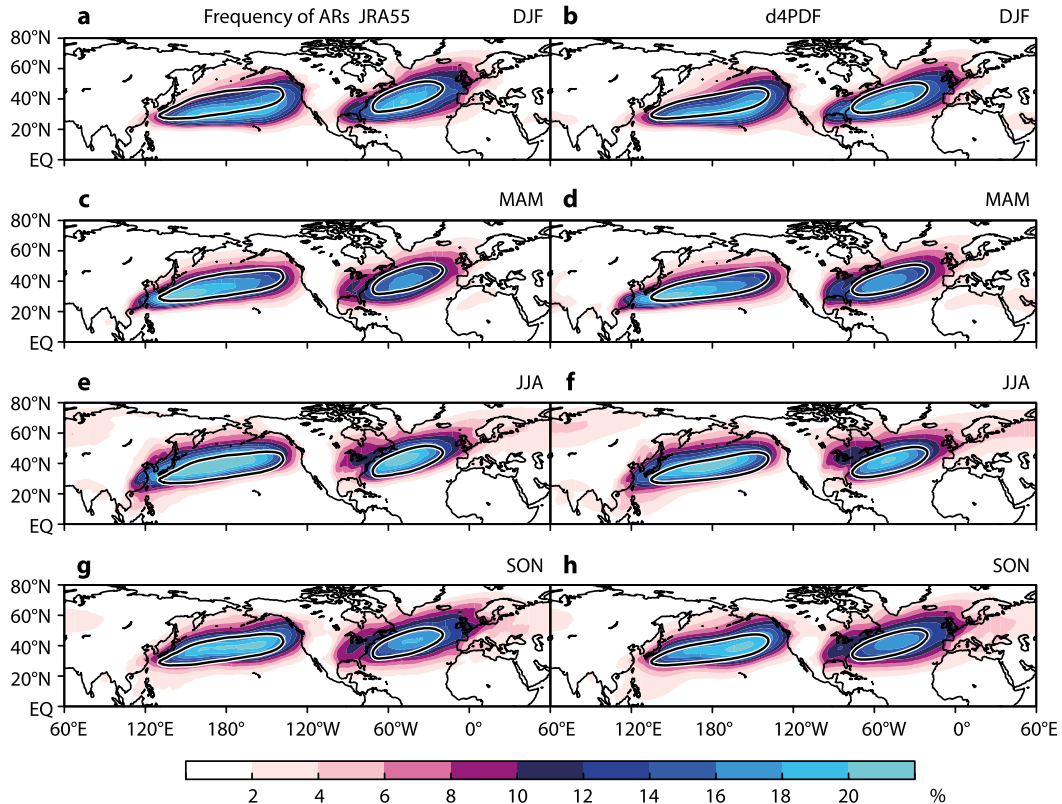
FIG. 2. Climatology (for 1958–2010) of seasonal-mean frequency (%) of ARs in the Northern Hemisphere. Averages for (a),(b) DJF, (c),(d) MAM, (e),(f) JJA, and (g),(h) SON from (left) JRA-55 and (right) 10-member ensemble mean of d4PDF historical simulations. Solid contours represent annual-mean frequency (14%).

d4PDF ensemble mean. The ARs are most frequent over the midlatitude (20°–60°N) central North Pacific and North Atlantic, consistent with previous studies (e.g., Guan and Waliser 2015; M16). The distributions of ARs and their peak occurrence show seasonal shifts in zonal and meridional directions. Over the North Pacific, AR frequency in December–February (DJF) is displaced southeastward from its annual mean, then shifts westward, northward and eastward in March–May (MAM), June–August (JJA), and September–November (SON), respectively. The peak position of AR frequency is found in the NWP (the western–central and central–eastern North Pacific) in MAM (JJA and SON). The frequency of landfalling AR also shows seasonal variation in accordance with the zonal and meridional shift of the climatological AR distribution (e.g., M16). Frequencies of AR landfalling over the west coast of North America and Europe peak in SON and DJF. In contrast, peaks of AR frequency are found in JJA and SON over northern Europe, eastern Europe, and western and northern Russia. ARs over the far eastern area of the Eurasian continent are most frequent in JJA. These seasonal variations are generally consistent

with previous studies (Guan and Waliser 2015; M16). The d4PDF ensemble mean (Figs. 2b,d,f,h) corresponds well with JRA-55, indicating that the AGCM can reproduce the mean AR frequency and its seasonal variation. Hereafter we mainly introduce results from the d4PDF because it has a larger sample size and thus shows more robust statistics than JRA-55.

Next we focus on ARs over the NWP and East Asia (Fig. 3). The ARs are broadly found all the seasons particularly over southern China and the Pacific coast of Japan. From DJF to MAM, the AR distribution shifts westward, substantially increasing over western Japan and southern China (Figs. 3a,b). The ARs concentrated in a narrow latitudinal band (20°–35°N) in DJF and MAM expand in the meridional direction in JJA, resulting in a substantial increase in AR frequency over Indochina, the South China Sea, and the Philippines in addition to northern Japan, the Korea Peninsula, and eastern Siberia (Fig. 3c). Frequency of landfalling ARs over the Eurasian continent is greatly reduced in SON. Figure 4 shows the frequency of ARs in JRA-55 and d4PDF averaged over the NWP region (25°–45°N, 125°–150°E; hereafter NWPARs) shown as rectangles in
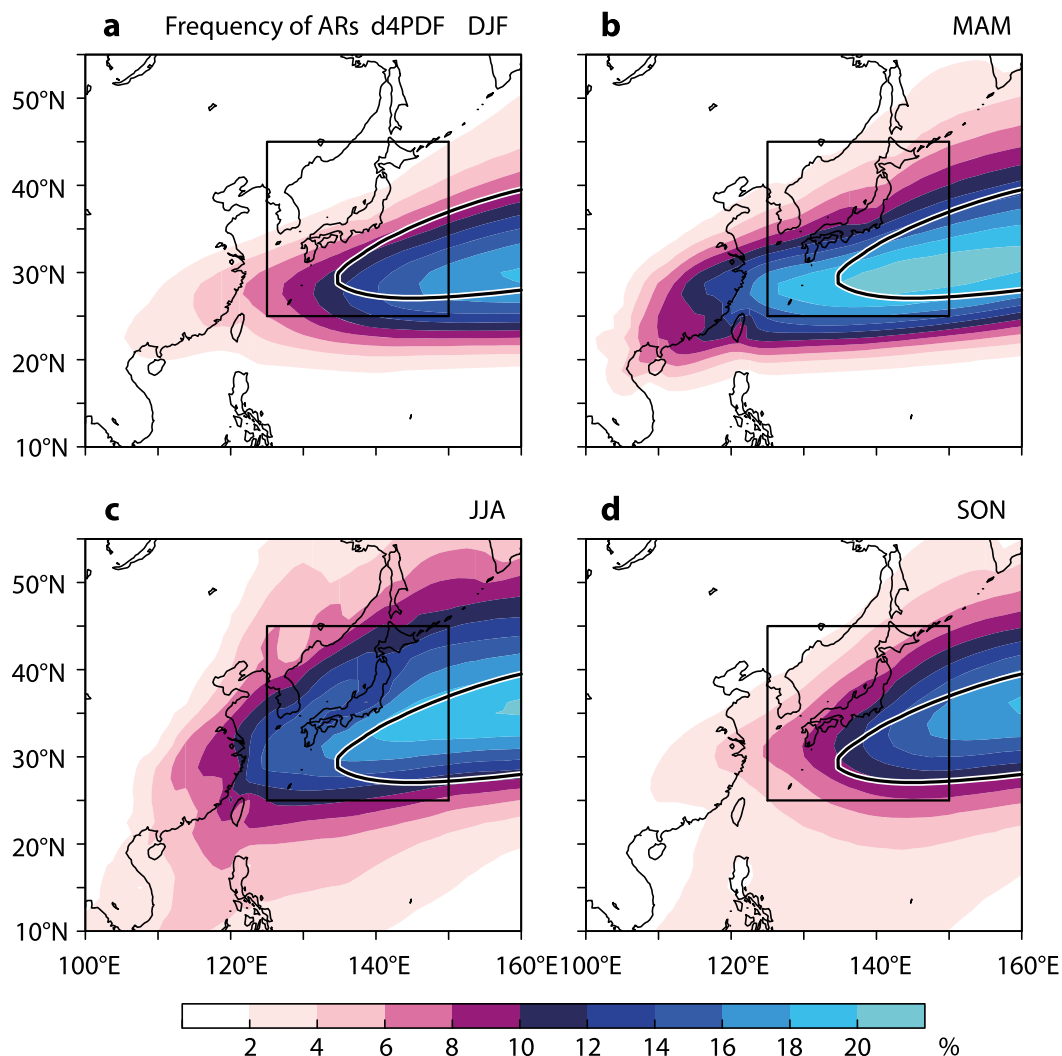
FIG. 3. As in Figs. 2b,d,f,h, but for East Asia. Black rectangles indicate the NWP region (25°–45°N, 125°–150°E, used in Figs. 4 and 6–8).

Fig. 3. The model reproduces seasonal variation of NWPARs with the maximum in June–July (13%–16%) and minimum in December (6%), similar to JRA-55. The interannual variability in 10-member ensemble mean in d4PDF (gray shading in Fig. 4) is smaller than that in JRA-55 (range between blue thin lines) because atmospheric internal variability is suppressed in the ensemble mean (Kamae et al. 2017). However, the interannual variability in the d4PDF ensemble mean is still substantial, suggesting the importance of forcing by SST variability (see section 4a).

Figure 5 shows seasonal variations of precipitation and AR frequency averaged over 125°–150°E. Here the AGCM can reproduce the detailed spatial distribution of EASM precipitation and its seasonal variation (Kusunoki 2017). Springtime precipitation peak at

29°–33°N (2–3 mm day^{-1}) is enhanced and shifts northward (33°–37°N) accompanied with the onset and the migration of the MB rainband (4–6 mm day^{-1}). ARs have their peak (at 27°–29°N) south of the rainband in MAM. In May–June, the maximum of AR occurrence shifts northward, concurrent with the MB rainband (at 31°N in June and at 36°–39°N in August). The ARs and MB rainband as a part of EASM show generally similar seasonal migration in June and July, but the ARs are also found during boreal winter and early spring, distinct from the EASM system. The summertime ARs are displaced south of the rainband, a meridional configuration consistent with observations that heavy rainfall events are accompanied with enormous transports of low-level water vapor from the south (e.g., Ninomiya and Akiyama 1992). In the next section, we examine
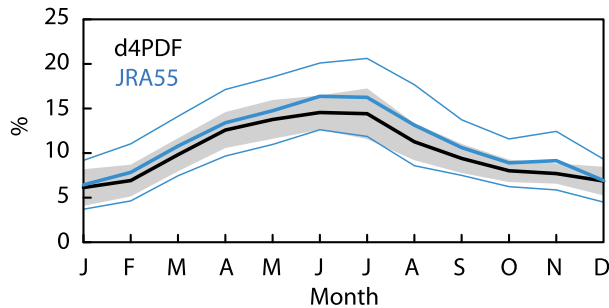
FIG. 4. Seasonal variation in monthly-mean climatology (for 1958–2010) of frequency of ARs (%) averaged over the NWP region (hereafter NWPARs). Thick blue and black lines represent JRA-55 and the 10-member ensemble mean of d4PDF. Range of thin blue lines and gray shading represent interannual variability (1σ) in JRA-55 and the ensemble mean of d4PDF.

interannual variability and potential predictability of NWPAR activity in JJA.

4. Interannual variability of AR frequency and atmospheric circulation

a. The northwestern Pacific ARs and SST

Figure 6 compares historical variations of NWPARs in JJA between JRA-55 and d4PDF. Here the 10-member ensemble mean (black line) and intermember spread of d4PDF (gray shading) indicate forced atmospheric response to SST and radiative forcing and unforced atmospheric variability, respectively (Kamae et al. 2017). The interannual variability in JRA-55 contains both forced and unforced variability, resulting in a larger variability than the d4PDF ensemble mean. The two time series (JRA-55 and ensemble mean d4PDF

time series) show statistically significant (at the 99.9% level) positive correlation ($R = 0.68$) for 1979–2010, indicating that 46% of interannual variability can be explained by the forced response. The correlation is limited ($R = 0.18$) before 1979, however, resulting in a lower correlation ($R = 0.33$) for 1958–2010 (but is still statistically significant at the 95% level) than 1979–2010. Relatively sparse observations assimilated to JRA-55 before 1979 (Kobayashi et al. 2015) may reduce the correlation. We should also note that this shift in the correlation is concurrent with interdecadal enhancements of ENSO amplitude and ENSO–EASM coupling since the late 1970s (Wu and Wang 2002; Wang et al. 2008; Xie et al. 2010; Chowdary et al. 2012; Kubota et al. 2016). The interdecadal variations of ARs are worth examining in future studies.

Guan and Waliser (2015) and M16 pointed out that the wintertime NWPARs are significantly affected by ENSO (i.e., more NWPARs during El Niño years). In contrast, the summertime NWPARs do not show a significant correlation ($R = -0.08$) with Niño-3.4 SST (5°S–5°N, 170°–120°W; yellow line in Fig. 6). Figure 7a shows a spatial pattern of the regression coefficient of SST with NWPARs in JJA. Here statistical tests are based on a 10-member ensemble of d4PDF historical simulations. While the correlation is insignificant over the equatorial Pacific (Figs. 6 and 7a), the north Indian Ocean (5°–25°N, 40°–100°E) SST (purple line in Fig. 6) correlates significantly (at the 99.9% level) with NWPARs ($R = 0.71$). Positive SST correlations with the NWPARs can be found over the tropical Indian Ocean, tropical Atlantic, and tropical southeastern Pacific (20°–5°S). This SST pattern resembles the summertime SST anomaly after El Niño (e.g., Fig. 7a in Xie et al. 2016). Figure 7b shows SST
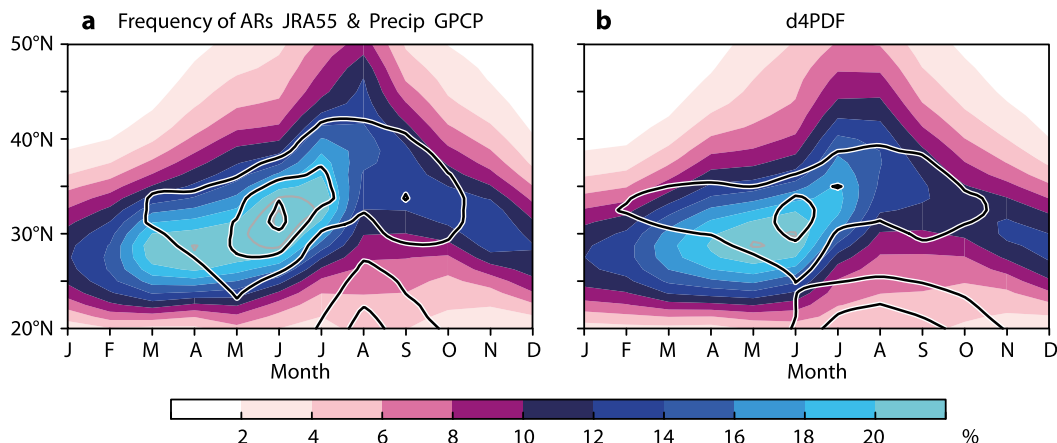

FIG. 5. Seasonal variations in monthly-mean climatologies of precipitation (black contours; 2, 4, and 6 mm day^{-1}) and AR frequency (shading; %) averaged over 125°–150°E from (a) Global Precipitation Climatology Project, version 2.2, and JRA-55 (1979–2010) and (b) d4PDF (1958–2010). Thin gray contours represent AR frequency of 22% and 24%.
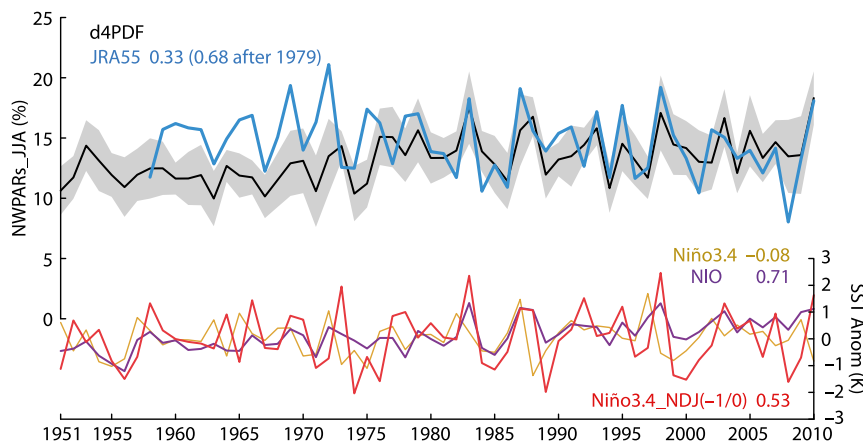
FIG. 6. Historical variations of JJA-mean NWPARs (%) and SST anomaly from the 1961–90 mean (K). Thick blue and black lines represent NWPARs from JRA-55 (for 1958–2010) and ensemble mean of d4PDF (for 1951–2010). Gray shading indicate 95% confidence interval. Yellow and purple lines represent SST anomalies averaged over the Niño-3.4 region (5°S–5°N, 170°–120°W) and north Indian Ocean (NIO; 5°–25°N, 40°–100°E), respectively. Red line represents preceding winter's [ND(−1)J(0) mean] Niño-3.4 SST. Values plotted indicate correlation coefficients with the ensemble mean of d4PDF.

regression during November–December of the preceding year and January of the target year [ND(−1)J(0)] on JJA(0) NWPARs. Here the numerals inside parentheses indicate the target year (0) and the preceding year (−1) of the summertime NWPARs. The NWPARs in JJA(0) correlate ($R = 0.53$) significantly (at the 99.9% level) with the preceding winter El Niño (Fig. 7b, red line in Fig. 6). This strong correlation suggests a substantial ENSO control on the following summer's NWPARs with a half-year lag. Figure 8 shows the lag correlation between JJA(0) NWPARs and SST. The Niño-3.4 SST (black lines in Fig. 8) shows a significant positive correlation in the preceding fall to winter both in d4PDF and JRA-55 ($R = 0.68$ and 0.47 in d4PDF and JRA-55,

respectively). The ENSO, particularly El Niño, tends to decay rapidly in the spring (e.g., Burgers and Stephenson 1999; An and Jin 2004; Ohba and Ueda 2009), resulting in the limited simultaneous correlation between the JJA(0) NWPARs and Niño-3.4 SST.

The above delayed response of the NWPARs to ENSO is consistent with the Indo–western Pacific Ocean capacitor (IPOC) effect (Xie et al. 2009, 2016). The brief concept of the IPOC effect and associated physical mechanisms were summarized as in Fig. 3 of Xie et al. (2016). During the El Niño winter, an anticyclonic circulation anomaly develops over the tropical western North Pacific (TWNP; 10°–20°N, 150°–170°E) through local air–sea interactions (Wang et al. 2000). Southwest

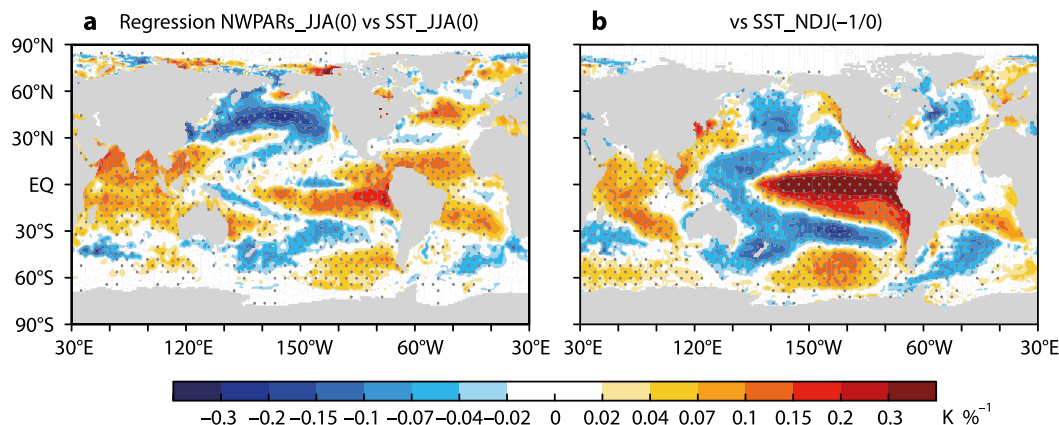FIG. 7. Spatial patterns of regression coefficients of (a) JJA(0) and (b) ND(−1)J(0) mean SST with JJA(0) mean NWPARs (K %$^{-1}$) in d4PDF 10-member ensemble. A 5-yr high-pass filter was applied before calculating regression coefficients. Stippling indicates the areas with 95% statistical confidence.
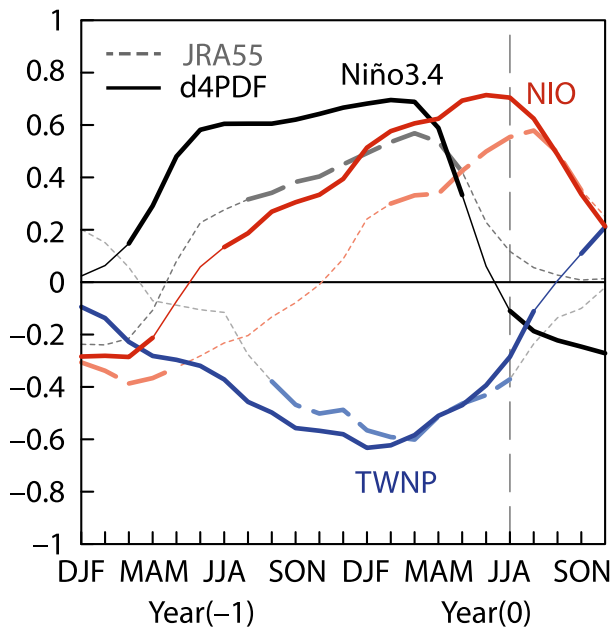
FIG. 8. Lagged correlations with JJA(0) mean NWPARs in the d4PDF 10-member ensemble (for 1951–2010; solid line) and JRA-55 (for 1958–2010; dashed line). A 5-yr high-pass filter was applied before calculating correlation coefficients. A vertical dashed line denotes JJA(0). Shown are 3-month running SST means for the Niño-3.4 region (black), north Indian Ocean (red), and TWNP (blue; 10°–20°N, 150°–170°E). Thick lines indicate the >95% confidence level.

Indian Ocean warming forced by El Niño acts to sustain the surface northwesterly anomaly over the north Indian Ocean during the following spring and early summer. The weakened monsoon southwesterly reduces evaporation from the sea surface, resulting in a north Indian Ocean warming (Du et al. 2009; Xie et al. 2009; Figs. 7 and 8). Eastward propagating equatorial Kelvin waves favored by the warm Indian Ocean (Yang et al. 2007) contribute to sustain the TWNP anticyclone during summer (see next subsection for detail). This IPOC mode affects the East Asian summer climate (e.g., Huang et al. 2004; Kosaka et al. 2013; Wang et al. 2013), manifested as the enhanced South Asian high (Yang et al. 2007), TWNP anticyclone (Wang et al. 2003, 2013), and meridional teleconnection initiated by convective activity around the Philippines (Nitta 1987; Kosaka and Nakamura 2010). In the next subsection, we show the relationships among the IPOC-related SST anomaly, EASM, and AR activity in post–El Niño summer. The significant correlation with Niño-3.4 SST of the preceding fall to winter (Figs. 7 and 8) indicates a potential predictability of the anomalous summertime NWPAR activity.

The ENSO effect on the summertime ARs is not limited to the NWP. Figure 9 shows regressions of JJA(0) ARs and low-level (at the 850-hPa level)

circulation on ND(−1)J(0) Niño-3.4 SST. Summer ARs in JRA-55 are more frequent over the midlatitude North Pacific and North Atlantic (Fig. 9a) after El Niño. The anomalous AR occurrence with low-level southwesterly anomaly (Fig. 9a) indicates a dynamically enhanced AR occurrence forced by El Niño. The positive anomaly is not limited to the central North Pacific and central North Atlantic but also includes other regions such as eastern China, the Pacific coast of Mexico, the east coast of North America, northern Europe, and the Laptev Sea. The results from the 10-member ensemble d4PDF are generally consistent with JRA-55 but more statistically significant (Fig. 9b), possibly because of reduced atmospheric noise. Over the NWP, the ARs are concentrated into a narrower latitudinal band (20°–40°N) after the El Niño than in normal years, resulting in a great increase (small decrease) over the Pacific coast of Japan (TWNP, northeastern China, and Sakhalin). The AR distribution expands southwestward in the North Pacific (and the North Atlantic), resulting in more ARs over Southeast Asia and southern China. The anomalous AR frequency is concurrent with the low-level circulation anomaly (more ARs are accompanied by anomalous southwesterlies, and vice versa), suggesting a monsoon control of the NWPARs (detailed in the next subsection).

b. Atmospheric circulation over the northwestern Pacific and Indian Ocean

In the previous subsection, we identified the spatial patterns of summer and preceding winter SST related to the interannual variability of summertime NWPARs (Fig. 7). Next we examine atmospheric circulation covariability over East Asia with the NWPARs. Figure 10 shows regressions of JJA(0) precipitation and atmospheric circulation on JJA(0) NWPARs. Generally the regression patterns suggest an enhanced EASM, with a stronger southwesterly monsoonal flow and precipitation over the South China Sea, the East China Sea, southern China, the Korea Peninsula, and Japan (Fig. 10a). This East Asian circulation pattern resembles the condition after El Niño (Fig. 9; e.g., Xie et al. 2016) due to the IPOC effect (Figs. 6–8). During the summers with more frequent NWPARs, SSTs over the north Indian Ocean and South China Sea tend to be higher than in normal years (Fig. 7a), resulting in the tropospheric warming over the Indian Ocean (Fig. 10b) and associated low-level anticyclone, easterly wind, and negative precipitation anomalies over the TWNP (Fig. 10a; Xie et al. 2009). In addition, the South Asian high and land–sea thermal contrast are enhanced (Fig. 10b), indicating a stronger EASM. During these years, seasonal-mean climate anomalies including the
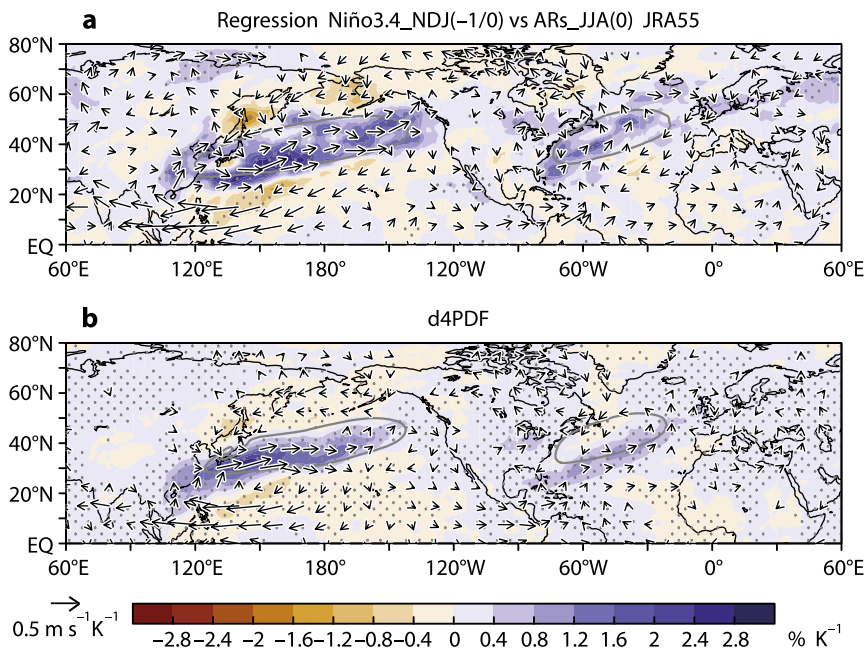
FIG. 9. Spatial patterns of regression coefficients of JJA(0) AR frequency (shading; % K^{-1}) and horizontal wind at the 850-hPa level (vector; m s^{-1} K^{-1}) in (a) JRA-55 and (b) d4PDF 10-member ensemble with ND(-1)J(0) Niño-3.4 SST. A 5-yr high-pass filter was applied. Gray contours represent climatology of AR frequency (14%). Stippling indicates the areas with 95% statistical confidence.

increased SST and the enhanced southwesterly monsoonal flow on the northwestern flank of the TWNP anticyclone facilitate more frequent occurrences of NWPARs (Fig. 9).

The increased summertime AR frequency after El Niño are concentrated in the narrow latitudinal band and expand southwestward to Southeast Asia and southern China (Fig. 9). This spatial pattern is consistent with the low-level circulation anomaly: the enhanced monsoonal southwesterly over the South China Sea, southern China, the East China Sea, and western Japan (Figs. 9 and 10a) associated with the TWNP anticyclonic anomaly (Fig. 10a). The anomalous TWNP anticyclone is consistent with the suppressed AR frequency over this region (Fig. 9). In the midlatitudes, the westerly wind anomaly is not found north of 40°N (Fig. 10a). The red line in Fig. 10a represents the latitude of the peak westerly wind regression onto the NWPARs. This axis is displaced south of the climatological westerly wind axis (gray line in Fig. 10a), suggesting that the low-level westerly axis shifts southward when the NWPARs are more frequent than in normal years. This southward shift is consistent with the suppressed AR activity north of 40°N (Fig. 9). Generally the anomalous pattern of summertime AR frequency over the Far East and the western Pacific are consistent with the anomalous circulation pattern, indicating the

importance of the ENSO-related EASM variability on the NWPAR interannual variability.

5. Summary and discussion

Using a global atmospheric reanalysis and a large-ensemble AGCM simulation, we have investigated the climatology and interannual variability of the summertime AR frequency over the Northern Hemisphere. The large-ensemble simulation contributes to identify the tropical mode controlling the interannual variability of the North Pacific ARs. ARs are broadly detected over the midlatitude oceans and make landfall not only over the west coasts of the Northern Hemisphere continents but also over East Asia. The NWPARs peak in June–July and make landfall over broad regions of the Far East including southern China and western Japan. The interannual variability of summertime NWPARs in JRA-55 is well reproduced by the AGCM ensemble mean, indicating the strong SST control. The interannual variability is closely related to the EASM strength modulated by Pacific and Indian Ocean SST anomalies. When El Niño develops in the equatorial Pacific during boreal winter, the IPOC mode influences the following summer atmospheric circulations over the Indian Ocean, the western North
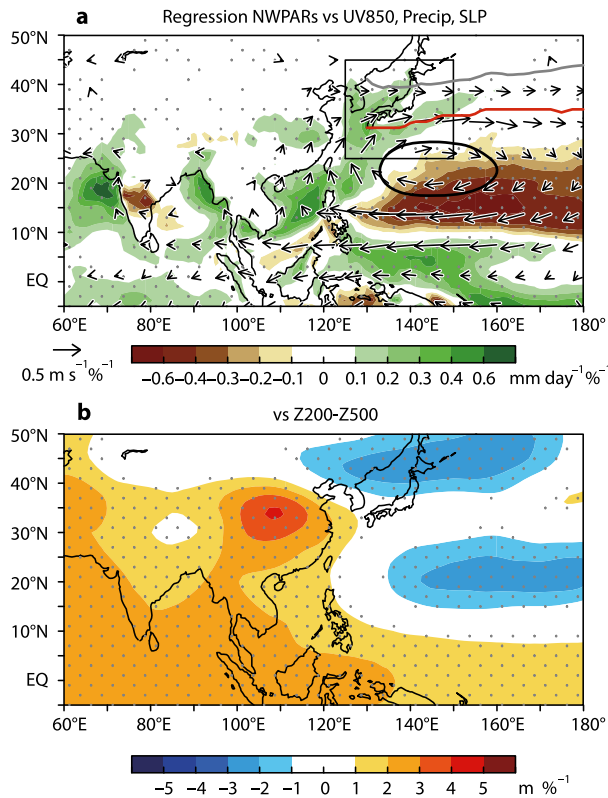
FIG. 10. Spatial patterns of regression coefficients with JJA NWPARs in d4PDF 10-member ensemble. A 5-yr high-pass filter was applied. (a) Precipitation (shading; mm day^{-1} %$^{-1}$), horizontal wind at the 850-hPa level (vector; m s^{-1} %$^{-1}$), and sea level pressure (contour; 0.4 hPa %$^{-1}$). Gray and red lines indicate the latitudes of the peak westerly wind at the 850-hPa level in climatology and in regression onto the NWPARs, respectively. Black rectangle indicates NWP region. (b) Regression coefficient of thickness between the 200- and 500-hPa levels (m %$^{-1}$). Stippling indicates the areas with 95% statistical confidence in (a) precipitation and (b) thickness.

Pacific, and East Asia at a half-year lag, producing a summertime anticyclonic circulation anomaly over the TWNP, an enhanced southwesterly monsoonal flow on the northwest flank, and frequent ARs over Southeast Asia, southern China, and western Japan. The high correlation between the summertime NWPARs and the Niño-3.4 index of the preceding winter indicates that modulations of summertime NWPAR activity and associated heavy rainfall over East Asia are highly predictable. Our results suggest that the probability of summertime heavy rainfall associated with AR-like features is increased over East Asia following El Niño events, while the risk of heavy rainfall associated with tropical cyclone landfall is reduced (e.g., Du et al. 2011; Mei et al. 2015). The seasonally lagged ENSO impacts on the ARs are important for the prediction of AR variability.

The summertime NWPAR activity is largely controlled by the atmosphere–ocean coupled mode over the tropical Indian Ocean and Pacific and is tied to the EASM variability, in contrast to the wintertime North Pacific and North Atlantic ARs that are affected by the jet stream, storm track, and Rossby wave breaking. Substantial parts of the summertime NWPARs are closely related to MB frontal activity (Fig. 1). However, AR-related heavy rainfall events also occurred after MB withdrawal (e.g., Hirota et al. 2016). This study only focuses on seasonal mean AR activity, but individual detected features suggest the complexity of the AR behavior over the western North Pacific (Knippertz and Wernli 2010; M16). The detection method employed in this study filters out tropical cyclones but retains narrow moisture transport bands associated with transitioning tropical cyclones. In addition, extratropical cyclones and NWPAR activities may also be affected remotely by tropical cyclones (e.g., Yoshida and Itoh 2012; Hirata and Kawamura 2014). These synoptic-scale features associated with the NWPAR activity are worthwhile to examine statistically. Moisture sources of the AR-like features are also essential for understanding formation mechanisms of ARs and its roles in the global hydrological cycle (e.g., Knippertz and Wernli 2010; Ramos et al. 2016). Hiraoka et al. (2011) and Pan et al. (2017) showed that moistures from the north Indian Ocean and the western North Pacific are major sources of the summertime rainfall over East Asia, but the contributions of moistures from other regions including the middle and high latitudes are also sizable. Further efforts at systematic classification of NWPAR events based on moisture sources and synoptic weather patterns (e.g., extratropical cyclones, tropical cyclones, MB front, and the North Pacific high; e.g., Ohba et al. 2015) may contribute to a better understanding of formation processes, climatology, variability, and socioeconomic impacts of NWPARs.

The AR statistics shown in this study may partly depend on detection methods. Guan and Waliser (2015) compared the performance of a detection scheme they developed and detection schemes employed in previous studies (Neiman et al. 2008; Lavers et al. 2011; Gorodetskaya et al. 2014). They concluded that different AR detection schemes showed good agreement (~90%) in AR landfall dates. They also pointed out a high sensitivity of IVT-based AR detection to length criterion (Fig. 5 in Guan and Waliser 2015). Despite these sensitivities, spatial patterns of the North Pacific AR climatology and its interannual variability (e.g., dependence on ENSO phases) are largely consistent among different studies (e.g., Guan and Waliser 2015; M16), suggesting a robustness of results shown in this study. It is worthwhile

to examine dependence of the AR behavior shown in this study to input data (Lavers et al. 2012; Guan and Waliser 2015) and criteria employed in the detection scheme (anomalous IVT threshold, length, and length–width ratio) under systematic framework.

This study focuses on the forced response to SST variability, but the unforced internal variability of ARs [see section 5 in Kamae et al. (2017)] also needs to be examined. The influences of the positions and strengths of extratropical cyclones, the upper-level jet stream, and Rossby wave breaking (e.g., Horinouchi 2014; Payne and Magnusdottir 2014) on the ARs over the western Pacific should also be investigated. The delayed impact of ENSO on summertime ARs is not limited to the NWP but is also found over North America, the North Atlantic, and Europe (e.g., more ARs over eastern North America and England; Fig. 9). In this study, we did not evaluate relative contributions of regional (e.g., the equatorial Pacific, the Indian Ocean, and the western North Pacific) and seasonal SST anomalies to the anomalous AR activity. More detailed research on the forced response to tropical SST variability and the internal variability of ARs is necessary for improved seasonal predictions of AR activity, associated water resource variations, and natural disasters.

This study only examines the frequency of AR occurrence. However, the AR strength, associated heavy rainfall, and their interannual variability are greatly important for risks of AR-related extreme events. In addition, future changes in these risks are also important topics. Water vapor increase resulting from atmospheric warming, shifts of the upper-level jet stream, and changes in low-level circulation patterns are important for the future changes in ARs (Lavers et al. 2013; Gao et al. 2015; Payne and Magnusdottir 2015; Hagos et al. 2016). Precipitable water over East Asia and the western Pacific is projected to increase in a warming climate (e.g., Endo and Kitoh 2014). Climate model simulations identified a long-term southward shift of the low-level westerly axis over the western Pacific (120°–150°E; e.g., Fig. 8 in Kitoh 2017). These thermodynamic and dynamic effects are likely to affect AR frequency and strength over the NWP. We plan to report on these changes in ARs and SST warming effect (Mizuta et al. 2017) in the near future.

REFERENCES

An, S.-I., and F.-F. Jin, 2004: Nonlinearity and asymmetry of ENSO. *J. Climate*, **17**, 2399–2412, doi:10.1175/1520-0442(2004)017<2399: NAAOE>2.0.CO;2.

Bao, J.-W., S. A. Michelson, P. J. Neiman, F. M. Ralph, and J. M. Wilczak, 2006: Interpretation of enhanced integrated water vapor bands associated with extratropical cyclones: Their formation and connection to tropical moisture. *Mon. Wea. Rev.*, **134**, 1063–1080, doi:10.1175/MWR3123.1.

Brands, S., J. M. Gutiérrez, and D. San-Martín, 2017: Twentieth-century atmospheric river activity along the west coasts of Europe and North America: Algorithm formulation, reanalysis uncertainty and links to atmospheric circulation patterns. *Climate Dyn.*, **48**, 2771–2795, doi:10.1007/s00382-016-3095-6.

Bueh, C., and H. Nakamura, 2007: Scandinavian pattern and its climatic impact. *Quart. J. Roy. Meteor. Soc.*, **133**, 2117–2131, doi:10.1002/qj.173.

Burgers, G., and D. B. Stephenson, 1999: The "normality" of El Niño. *Geophys. Res. Lett.*, **26**, 1027–1030, doi:10.1029/1999GL900161.

Chowdary, J. S., S.-P. Xie, H. Tokinaga, Y. M. Okumura, H. Kubota, N. Johnson, and X.-T. Zheng, 2012: Interdecadal variations in ENSO teleconnection to the Indo–western Pacific for 1870–2007. *J. Climate*, **25**, 1722–1744, doi:10.1175/JCLI-D-11-00070.1.

Dettinger, M. D., 2013: Atmospheric rivers as drought busters on the U.S. West Coast. *J. Hydrometeor.*, **14**, 1721–1732, doi:10.1175/JHM-D-13-02.1.

——, F. M. Ralph, T. Das, P. J. Neiman, and D. R. Cayan, 2011: Atmospheric rivers, floods, and the water resources of California. *Water*, **3**, 445–478, doi:10.3390/w3020445.

Ding, Y., and J. C. L. Chan, 2005: The East Asian summer monsoon: An overview. *Meteor. Atmos. Phys.*, **89**, 117–142, doi:10.1007/s00703-005-0125-z.

Du, Y., S.-P. Xie, G. Huang, and K. M. Hu, 2009: Role of air–sea interaction in the long persistence of El Niño–induced north Indian Ocean warming. *J. Climate*, **22**, 2023–2038, doi:10.1175/2008JCLI2590.1.

——, L. Yang, and S.-P. Xie, 2011: Tropical Indian Ocean influence on northwest Pacific tropical cyclones in summer following strong El Niño. *J. Climate*, **24**, 315–322, doi:10.1175/2010JCLI3890.1.

Endo, H., and A. Kitoh, 2014: Thermodynamic and dynamic effects on regional monsoon rainfall changes in a warmer climate. *Geophys. Res. Lett.*, **41**, 1704–1710, doi:10.1002/2013GL059158.

Gao, Y., J. Lu, L. R. Leung, Q. Yang, S. Hagos, and Y. Qian, 2015: Dynamical and thermodynamical modulations on future changes of landfalling atmospheric rivers over western North America. *Geophys. Res. Lett.*, **42**, 7179–7186, doi:10.1002/2015GL065435.

Gimeno, L., R. Nieto, M. Vázquez, and D. A. Lavers, 2014: Atmospheric rivers: A mini-review. *Front. Earth Sci.*, **2**, 2.1–2.6, doi:10.3389/feart.2014.00002.

——, and Coauthors, 2016: Major mechanisms of atmospheric moisture transport and their role in extreme precipitation

events. *Annu. Rev. Environ. Resour.*, **41**, 117–141, doi:10.1146/annurev-environ-110615-085558.

Gorodetskaya, I. V., M. Tsukernik, K. Claes, M. F. Ralph, W. D. Neff, and N. P. M. Van Lipzig, 2014: The role of atmospheric rivers in anomalous snow accumulation in East Antarctica. *Geophys. Res. Lett.*, **41**, 6199–6206, doi:10.1002/2014GL060881.

Guan, B., and D. E. Waliser, 2015: Detection of atmospheric rivers: Evaluation and application of an algorithm for global studies. *J. Geophys. Res. Atmos.*, **120**, 12 514–12 535, doi:10.1002/2015JD024257.

Hagos, S. M., L. R. Leung, J.-H. Yoon, J. Lu, and Y. Gao, 2016: A projection of changes in landfalling atmospheric river frequency and extreme precipitation over western North America from the large ensemble CESM simulations. *Geophys. Res. Lett.*, **43**, 1357–1363, doi:10.1002/2015GL067392.

Hirahara, S., M. Ishii, and Y. Fukuda, 2014: Centennial-scale sea surface temperature analysis and its uncertainty. *J. Climate*, **27**, 57–75, doi:10.1175/JCLI-D-12-00837.1.

Hiraoka, A., R. Kawamura, K. Ichiyanagi, M. Tanoue, and K. Yoshimura, 2011: Water origins in central and southern Japan during early summer rainy season as simulated with an isotope circulation model. *SOLA*, **7**, 141–144, doi:10.2151/sola.2011-036.

Hirata, H., and R. Kawamura, 2014: Scale interaction between typhoons and the North Pacific subtropical high and associated remote effects during the Baiu/Meiyu season. *J. Geophys. Res. Atmos.*, **119**, 5157–5170, doi:10.1002/2013JD021430.

Hirota, N., Y. N. Takayabu, M. Kato, and S. Arakane, 2016: Roles of an atmospheric river and a cutoff low in the extreme precipitation event in Hiroshima on 19 August 2014. *Mon. Wea. Rev.*, **144**, 1145–1160, doi:10.1175/MWR-D-15-0299.1.

Horinouchi, T., 2014: Influence of upper tropospheric disturbances on the synoptic variability of precipitation and moisture transport over summertime East Asia and the northwestern Pacific. *J. Meteor. Soc. Japan*, **92**, 519–541, doi:10.2151/jmsj.2014-602.

Huang, R., W. Chen, B. Yang, and R. Zhang, 2004: Recent advances in studies of the interaction between the East Asian winter and summer monsoons and ENSO cycle. *Adv. Atmos. Sci.*, **21**, 407–424, doi:10.1007/BF02915568.

——, J. Chen, and G. Huang, 2007: Characteristics and variations of the East Asian monsoon system and its impacts on climate disasters in China. *Adv. Atmos. Sci.*, **24**, 993–1023, doi:10.1007/s00376-007-0993-x.

Huffman, G. J., R. F. Adler, D. T. Bolvin, and G. Gu, 2009: Improving the global precipitation record: GPCP version 2.1. *Geophys. Res. Lett.*, **36**, L17808, doi:10.1029/2009GL040000.

Jackson, D. L., M. Hughes, and G. A. Wick, 2016: Evaluation of landfalling atmospheric rivers along the U.S. West Coast in reanalysis data sets. *J. Geophys. Res. Atmos.*, **121**, 2705–2718, doi:10.1002/2015JD024412.

Kamae, Y., and Coauthors, 2017: Forced response and internal variability of summer climate over western North America. *Climate Dyn.*, doi:10.1007/s00382-016-3350-x, in press.

Kamiguchi, K., O. Arakawa, A. Kitoh, A. Yatagai, A. Hamada, and N. Yasutomi, 2010: Development of APHRO_JP, the first Japanese high-resolution daily precipitation product for more than 100 years. *Hydrol. Res. Lett.*, **4**, 60–64, doi:10.3178/hrl.4.60.

Khouakhi, A., and G. Villarini, 2016: On the relationship between atmospheric rivers and high sea water levels along the U.S. West Coast. *Geophys. Res. Lett.*, **43**, 8815–8822, doi:10.1002/2016GL070086.

Kitoh, A., 2017: The Asian monsoon and its future change in climate models: A review. *J. Meteor. Soc. Japan*, **95**, 7–33, doi:10.2151/jmsj.2017-002.

Knippertz, P., and H. Wernli, 2010: A Lagrangian climatology of tropical moisture exports to the Northern Hemispheric extratropics. *J. Climate*, **23**, 987–1003, doi:10.1175/2009JCLI3333.1.

Kobayashi, S., and Coauthors, 2015: The JRA-55 Reanalysis: General specifications and basic characteristics. *J. Meteor. Soc. Japan*, **93**, 5–48, doi:10.2151/jmsj.2015-001.

Kodama, Y.-M., 1993: Large-scale common features of subtropical convergence zones (the baiu frontal zone, the SPCZ, and the SACZ). Part II: Conditions of the circulations for generating the STCZs. *J. Meteor. Soc. Japan*, **71**, 581–610.

Kosaka, Y., and H. Nakamura, 2010: Mechanisms of meridional teleconnection observed between a summer monsoon system and a subtropical anticyclone. Part I: The Pacific–Japan pattern. *J. Climate*, **23**, 5085–5108, doi:10.1175/2010JCLI3413.1.

——, S.-P. Xie, N.-C. Lau, and G. A. Vecchi, 2013: Origin of seasonal predictability for summer climate over the northwestern Pacific. *Proc. Natl. Acad. Sci. USA*, **110**, 7574–7579, doi:10.1073/pnas.1215582110.

Kubota, H., Y. Kosaka, and S.-P. Xie, 2016: A 117-year long index of the Pacific-Japan pattern with application to interdecadal variability. *Int. J. Climatol.*, **36**, 1575–1589, doi:10.1002/joc.4441.

Kusunoki, S., 2017: Is the global atmospheric model MRI-AGCM3.2 better than the CMIP5 atmospheric models in simulating precipitation over East Asia? *Climate Dyn.*, doi:10.1007/s00382-016-3335-9, in press.

Lau, K.-M., and S. Yang, 1997: Climatology and interannual variability of the Southeast Asian summer monsoon. *Adv. Atmos. Sci.*, **14**, 141–162, doi:10.1007/s00376-997-0016-y.

Lavers, D. A., R. P. Allan, E. F. Wood, G. Villarini, D. J. Brayshaw, and A. J. Wade, 2011: Winter floods in Britain are connected to atmospheric rivers. *Geophys. Res. Lett.*, **38**, L23803, doi:10.1029/2011GL049783.

——, ——, ——, and A. J. Wade, 2012: The detection of atmospheric rivers in atmospheric reanalyses and their links to British winter floods and the large-scale climatic circulation. *J. Geophys. Res.*, **117**, D20106, doi:10.1029/2012JD018027.

——, ——, G. Villarini, B. Lloyd-Hughes, D. J. Brayshaw, and A. J. Wade, 2013: Future changes in atmospheric rivers and their implications for winter flooding in Britain. *Environ. Res. Lett.*, **8**, 034010, doi:10.1088/1748-9326/8/3/034010.

——, F. Pappenberger, and E. Zsoter, 2014: Extending medium-range predictability of extreme hydrological events in Europe. *Nat. Commun.*, **5**, 5382, doi:10.1038/ncomms6382.

Mailier, P. J., D. B. Stephenson, C. A. T. Ferro, and K. I. Hodges, 2006: Serial clustering of extratropical cyclones. *Mon. Wea. Rev.*, **134**, 2224–2240, doi:10.1175/MWR3160.1.

Manda, A., and Coauthors, 2014: Impacts of a warming marginal sea on torrential rainfall organized under the Asian summer monsoon. *Sci. Rep.*, **4**, 5741, doi:10.1038/srep05741.

Matsumoto, S., K. Ninomiya, and S. Yoshizumi, 1971: Characteristic features of ''Baiu'' front associated with heavy rainfall. *J. Meteor. Soc. Japan*, **49**, 267–281, doi:10.2151/jmsj1965.49.4_267.

Mei, W., S.-P. Xie, M. Zhao, and Y. Wang, 2015: Forced and internal variability of tropical cyclone track density in the western North Pacific. *J. Climate*, **28**, 143–167, doi:10.1175/JCLI-D-14-00164.1.

Mizuta, R., and Coauthors, 2012: Climate simulations using MRI-AGCM with 20-km grid. *J. Meteor. Soc. Japan*, **90A**, 233–258, doi:10.2151/jmsj.2012-A12.

——, and Coauthors, 2017: Over 5000 years of ensemble future climate simulations by 60-km global and 20-km regional atmospheric models. *Bull. Amer. Meteor. Soc.*, 10.1175/BAMS-D-16-0099.1, in press.

Mundhenk, B. D., E. A. Barnes, and E. D. Maloney, 2016: All-season climatology and variability of atmospheric river frequencies over the North Pacific. *J. Climate*, **29**, 4885–4903, doi:10.1175/JCLI-D-15-0655.1.

Murakami, H., R. Mizuta, and E. Shindo, 2012: Future changes in tropical cyclone activity projected by multi-physics and multi-SST ensemble experiments using the 60-km-mesh MRI-AGCM. *Climate Dyn.*, **39**, 2569–2584, doi:10.1007/s00382-011-1223-x.

National Geophysical Data Center, 2006: 2-minute gridded global relief data (ETOPO2) v2. NOAA/National Centers for Environmental Information, accessed 15 February 2017, doi:10.7289/V5J1012Q.

Nayak, M. A., G. Villarini, and D. A. Lavers, 2014: On the skill of numerical weather prediction models to forecast atmospheric rivers over the central United States. *Geophys. Res. Lett.*, **41**, 4354–4362, doi:10.1002/2014GL060299.

Neiman, P. J., F. M. Ralph, G. A. Wick, J. D. Lundquist, and M. D. Dettinger, 2008: Meteorological characteristics and overland precipitation impacts of atmospheric rivers affecting the west coast of North America based on eight years of SSM/I satellite observations. *J. Hydrometeor.*, **9**, 22–47, doi:10.1175/2007JHM855.1.

Ninomiya, K., 1980: Enhancement of Asian subtropical front due to thermodynamic effect of cumulus convections. *J. Meteor. Soc. Japan*, **58**, 1–15, doi:10.2151/jmsj1965.58.1_1.

——, and T. Murakami, 1987: The early summer rainy season (Baiu) over Japan. *Monsoon Meteorology*, C.-P. Chang and T. N. Krishnamurti, Eds., Oxford University Press, 93–121.

——, and T. Akiyama, 1992: Multi-scale features of Baiu, the summer monsoon over Japan and the East Asia. *J. Meteor. Soc. Japan*, **70**, 467–495, doi:10.2151/jmsj1965.70.1B_467.

——, and Y. Shibagaki, 2007: Multi-scale features of the Meiyu-Baiu front and associated precipitation systems. *J. Meteor. Soc. Japan*, **85B**, 103–122, doi:10.2151/jmsj.85B.103.

Nitta, T., 1987: Convective activities in the tropical western Pacific and their impact on the Northern Hemisphere summer circulation. *J. Meteor. Soc. Japan*, **65**, 373–390, doi:10.2151/jmsj1965.65.3_373.

Ohba, M., and H. Ueda, 2009: Role of nonlinear atmospheric response to SST on the asymmetric transition process of ENSO. *J. Climate*, **22**, 177–192, doi:10.1175/2008JCLI2334.1.

——, S. Kadokura, Y. Yoshida, D. Nohara, and Y. Toyoda, 2015: Anomalous weather patterns in relation to heavy precipitation events in Japan during the baiu season. *J. Hydrometeor.*, **16**, 688–701, doi:10.1175/JHM-D-14-0124.1.

Pan, C., B. Zhu, J. Gao, and H. Kang, 2017: Source apportionment of atmospheric water over East Asia—A source tracer study in CAM5.1. *Geosci. Model Dev.*, **10**, 673–688, doi:10.5194/gmd-10-673-2017.

Payne, A. E., and G. Magnusdottir, 2014: Dynamics of landfalling atmospheric rivers over the North Pacific in 30 years of MERRA reanalysis. *J. Climate*, **27**, 7133–7150, doi:10.1175/JCLI-D-14-00034.1.

——, and ——, 2015: An evaluation of atmospheric rivers over the North Pacific in CMIP5 and their response to warming under RCP 8.5. *J. Geophys. Res. Atmos.*, **120**, 11 173–11 190, doi:10.1002/2015JD023586.

Ralph, F. M., P. J. Neiman, and G. A. Wick, 2004: Satellite and CALJET aircraft observations of atmospheric rivers over the eastern North Pacific Ocean during the winter of 1997/98. *Mon. Wea. Rev.*, **132**, 1721–1745, doi:10.1175/1520-0493(2004)132<1721:SACAOO>2.0.CO;2.

Ramos, A. M., R. Nieto, R. Tomé, L. Gimeno, R. M. Trigo, M. L. R. Liberato, and D. A. Lavers, 2016: Atmospheric rivers moisture sources from a Lagrangian perspective. *Earth Syst. Dyn.*, **7**, 371–384, doi:10.5194/esd-7-371-2016.

Rayner, N. A., D. E. Parker, E. B. Horton, C. K. Folland, L. V. Alexander, D. P. Rowell, E. C. Kent, and A. Kaplan, 2003: Global analyses of sea surface temperature, sea ice, and night marine air temperature since the late nineteenth century. *J. Geophys. Res.*, **108**, 4407, doi:10.1029/2002JD002670.

Sampe, T., and S.-P. Xie, 2010: Large-scale dynamics of the meiyu-baiu rain band: Environmental forcing by the westerly jet. *J. Climate*, **23**, 113–134, doi:10.1175/2009JCLI3128.1.

Tao, S., and L. Chen, 1987: A review of recent research on the East Asian summer monsoon in China. *Monsoon Meteorology*, C.-P. Chang and T. N. Krishnamurti, Eds., Oxford University Press, 60–92.

Ueda, H., 2005: Air–sea coupled process involved in stepwise seasonal evolution of the Asian summer monsoon. *Geogr. Rev. Japan*, **78**, 825–841, doi:10.4157/grj.78.825.

——, T. Yasunari, and R. Kawamura, 1995: Abrupt seasonal change of large-scale convective activity over the western Pacific in the northern summer. *J. Meteor. Soc. Japan*, **73**, 795–809.

Viale, M., and M. N. Nuñez, 2011: Climatology of winter orographic precipitation over the subtropical central Andes and associated synoptic and regional characteristics. *J. Hydrometeor.*, **12**, 481–507, doi:10.1175/2010JHM1284.1.

Waliser, D., and B. Guan, 2017: Extreme winds and precipitation during landfall of atmospheric rivers. *Nat. Geosci.*, **10**, 179–183, doi:10.1038/ngeo2894.

Wang, B., and LinHo, 2002: Rainy season of the Asian-Pacific summer monsoon. *J. Climate*, **15**, 386–398, doi:10.1175/1520-0442(2002)015<0386:RSOTAP>2.0.CO;2.

——, R. Wu, and X. Fu, 2000: Pacific–East Asia teleconnection: How does ENSO affect East Asian climate? *J. Climate*, **13**, 1517–1536, doi:10.1175/1520-0442(2000)013<1517:PEATHD>2.0.CO;2.

——, ——, and T. Li, 2003: Atmosphere–warm ocean interaction and its impacts on Asian-Australian monsoon variation. *J. Climate*, **16**, 1195–1211, doi:10.1175/1520-0442(2003)16<1195:AOIAII>2.0.CO;2.

——, J. Yang, T. Zhou, and B. Wang, 2008: Interdecadal changes in the major modes of Asian–Australian monsoon variability: Strengthening relationship with ENSO since the late 1970s. *J. Climate*, **21**, 1771–1789, doi:10.1175/2007JCLI1981.1.

——, B. Xiang, and J.-Y. Lee, 2013: Subtropical high predictability establishes a promising way for monsoon and tropical storm predictions. *Proc. Natl. Acad. Sci. USA*, **110**, 2718–2722, doi:10.1073/pnas.1214626110.

Wang, Y., 1992: Effects of blocking anticyclones in Eurasia in the rainy season (Meiyu/Baiu season). *J. Meteor. Soc. Japan*, **70**, 929–951, doi:10.2151/jmsj1965.70.5_929.

Wick, G. A., P. J. Neiman, F. M. Ralph, and T. M. Hamill, 2013: Evaluation of forecasts of the water vapor signature of atmospheric rivers in operational numerical weather prediction models. *Wea. Forecasting*, **28**, 1337–1352, doi:10.1175/WAF-D-13-00025.1.

Wu, R., and B. Wang, 2002: A contrast of the East Asian summer monsoon–ENSO relationship between 1962–77 and 1978–93. *J. Climate*, **15**, 3266–3279, doi:10.1175/1520-0442(2002)015<3266: ACOTEA>2.0.CO;2.

Xie, S.-P., and N. Saiki, 1999: Abrupt onset and slow seasonal evolution of summer monsoon in an idealized GCM simulation. *J. Meteor. Soc. Japan*, **77**, 949–968, doi:10.2151/ jmsj1965.77.4_949.

——, K. Hu, J. Hafner, H. Tokinaga, Y. Du, G. Huang, and T. Sampe, 2009: Indian Ocean capacitor effect on Indo-western Pacific climate during the summer following El Niño. *J. Climate*, **22**, 730–747, doi:10.1175/ 2008JCLI2544.1.

——, Y. Du, G. Huang, X.-T. Zheng, H. Tokinaga, K. M. Hu, and Q. Y. Liu, 2010: Decadal shift in El Niño influences on Indo–western Pacific and East Asian climate in the 1970s. *J. Climate*, **23**, 3352–3368, doi:10.1175/2010JCLI3429.1.

——, Y. Kosaka, Y. Du, K. Hu, J. S. Chowdary, and G. Huang, 2016: Indo-western Pacific ocean capacitor and coherent climate anomalies in post-ENSO summer: A review. *Adv. Atmos. Sci.*, **33**, 411–432, doi:10.1007/s00376-015-5192-6.

Yang, J., Q. Liu, S. Xie, Z. Liu, and L. Wu, 2007: Impact of the Indian Ocean SST basin mode on the Asian summer monsoon. *Geophys. Res. Lett.*, **34**, L02708, doi:10.1029/2006GL028571.

Yoshida, K., and H. Itoh, 2012: Indirect effects of tropical cyclones on heavy rainfall events in Kyushu, Japan, during the Baiu season. *J. Meteor. Soc. Japan*, **90**, 377–401, doi:10.2151/ jmsj.2012-303.

Zhu, Y., and R. E. Newell, 1998: A proposed algorithm for moisture fluxes from atmospheric rivers. *Mon. Wea. Rev.*, **126**, 725–735, doi:10.1175/1520-0493(1998)126<0725:APAFMF>2.0.CO;2.